Opto-Electronic Science

ISSN 2097-0382 CN 51-1800/O4

Hybrid bound states in the continuum in terahertz metasurfaces

Junxing Fan, Zuolong Li, Zhanqiang Xue, Hongyang Xing, Dan Lu, Guizhen Xu, Jianqiang Gu, Jiaguang Han and Longqing Cong

Citation: Fan JX, Li ZL, Xue ZQ, Xing HY, Lu D et al. Hybrid bound states in the continuum in terahertz metasurfaces. *Opto Electron Sci* **2**, 230006 (2023).

Received: 3 February 2023; Accepted: 24 April 2023; Published online: 18 May 2023

Related articles

High-*Q* resonances governed by the quasi-bound states in the continuum in all-dielectric metasurfaces

Cizhe Fang, Qiyu Yang, Qingchen Yuan, Xuetao Gan, Jianlin Zhao, Yao Shao, Yan Liu, Genquan Han, Yue Hao

Opto-Electronic Advances 2021 **4**, 200030 doi: 10.29026/oea.2021.200030

Terahertz metasurface zone plates with arbitrary polarizations to a fixed polarization conversion

Zhen Yue, Jitao Li, Jie Li, Chenglong Zheng, Jingyu Liu, Guocui Wang, Hang Xu, Mingyang Chen, Yating Zhang, Yan Zhang, Jianquan Yao

Opto-Electronic Science 2022 **1**, 210014 doi: 10.29026/oes.2022.210014

Multi-cycle reconfigurable THz extraordinary optical transmission using chalcogenide metamaterials

Tun Cao, Meng Lian, Xieyu Chen, Libang Mao, Kuan Liu, Jingyuan Jia, Ying Su, Haonan Ren, Shoujun Zhang, Yihan Xu, Jiajia Chen, Zhen Tian, Dongming Guo

Opto-Electronic Science 2022 **1**, 210010 doi: 10.29026/oes.2022.210010

Dual bound states in the continuum enhanced second harmonic generation with transition metal dichalcogenides monolayer

Peilong Hong, Lei Xu, Mohsen Rahmani

Opto-Electronic Advances 2022 **5**, 200097 doi: 10.29026/oea.2022.200097

Opto-Electronic Science

Article

April 2023, Vol. 2, No. 4

DOI: 10.29026/oes.2023.230006

Hybrid bound states in the continuum in terahertz metasurfaces

Junxing Fan[1], Zuolong Li[2], Zhanqiang Xue[1], Hongyang Xing[1], Dan Lu[1], Guizhen Xu[1], Jianqiang Gu[2]*, Jiaguang Han[2,3]* and Longqing Cong[1]*

Bound states in the continuum (BICs) have exhibited extraordinary properties in photonics for enhanced light-matter interactions that enable appealing applications in nonlinear optics, biosensors, and ultrafast optical switches. The most common strategy to apply BICs in a metasurface is by breaking symmetry of resonators in the uniform array that leaks the otherwise uncoupled mode to free space and exhibits an inverse quadratic relationship between quality factor (*Q*) and asymmetry. Here, we propose a scheme to further reduce scattering losses and improve the robustness of symmetry-protected BICs by decreasing the radiation density with a hybrid BIC lattice. We observe a significant increase of radiative *Q* in the hybrid lattice compared to the uniform lattice with a factor larger than 14.6. In the hybrid BIC lattice, modes are transferred to *Γ* point inherited from high symmetric *X*, *Y*, and *M* points in the Brillouin zone that reveal as multiple Fano resonances in the far field and would find applications in hyperspectral sensing. This work initiates a novel and generalized path toward reducing scattering losses and improving the robustness of BICs in terms of lattice engineering that would release the rigid requirements of fabrication accuracy and benefit applications of photonics and optoelectronic devices.

Keywords: bound states in the continuum; metasurfaces; terahertz photonics; radiative losses; Fano resonances

Fan JX, Li ZL, Xue ZQ, Xing HY, Lu D et al. Hybrid bound states in the continuum in terahertz metasurfaces. *Opto-Electron Sci* **2**, 230006 (2023).

Introduction

Resonant cavities can effectively confine light and enhance light-matter interactions, which are of great importance to technologies and applications including lasers[1–4], filters[5,6], harmonic generation[7–11], and sensors[12,13]. Quality factor (*Q*) is one of the most important parameters to characterize the strength of light-matter interactions. Different schemes have been proposed to improve *Q* in microcavities[14], such as microdisks[15,16], Bragg reflector microcavities[17], and photonic crystals[18]. In the same context, a generalized concept of bound states in the continuum (BIC) was raised[19–21], which is in fact a topological defect in the momentum space and localizes in the continuous spectrum of extended states but is unable to couple to free space. Therefore, an ideal BIC will theoretically exhibit an infinite lifetime. Since the first demonstration, BICs have been applied to improve the performance in a plethora of optical applications by opening a coupling channel to free space via symmetry breaking of unit cells. Although any value of *Q* could be

[1]Department of Electrical and Electronic Engineering, Southern University of Science and Technology, Shenzhen 518055, China; [2]Center for Terahertz Waves and College of Precision Instrument and Optoelectronics Engineering, Tianjin University, Tianjin 300072, China; [3]Guangxi Key Laboratory of Optoelectronic Information Processing, School of Optoelectronic Engineering, Guilin University of Electronic Technology, Guilin 541004, China.

Received: 3 February 2023; Accepted: 24 April 2023; Published online: 18 May 2023

theoretically obtained, the measured values are commonly much lower than their theoretical predictions due to unavoidable scattering losses by fabrication defects, finite size of resonator array, and Ohmic losses in practice[22–24]. One solution to reduce the susceptibility of BIC to defect-induced scattering losses is by merging multiple BICs in the vicinity of Γ point in the Brillouin zone (BZ) that in fact decreases the slope of radiative Q versus wavevector (k) from an inverse quadratic relationship ($Q_{\rm rad} \propto k^{-2}$) to a higher order (e.g., $Q_{\rm rad} \propto k^{-6}$) and thus improves the rubustness[25–27]. This is a smart strategy to access a stable and high Q resonance; however, a large number of complex calculations and subnanometer geometrical accuracy of resonators are required to guarantee the merged states, and a special band is demanded that must possess multiple BICs at Γ point as well as off-Γ points (accidental BICs).

Here, we introduce a generalized scheme to access robust and high-Q BICs by decreasing the radiation density in a *hybrid* metasurface lattice. For a common lattice supporting symmetry-protected BICs, the leaky channel is opened by uniformly breaking the symmetry of resonators in the unit cell, while a *hybrid lattice* indicates that half or a quarter (or less) of resonators in a supercell are symmetry breaking so that the radiation density reduces in the lattice. In the course of radiation suppression, the radiative Q versus k will theoretically have a 16-time larger coefficient in a 1/4 hybrid lattice compared to the common BICs that would enable a robust high-Q resonance. The idea was numerically and experimentally demonstrated by an array of classical double-gap split ring resonators (DSRR) with C_2 symmetry in terahertz regime that supports symmetry-protected BICs[28]. Band folding analysis in BZ was performed to visualize the evolution of modes and quality factors between *uniform* and *hybrid* lattices. In the hybrid lattice, the high-Q portion of band was retained from the uniform lattice, while the low-Q portion was discarded in the band folding process resulting in a relatively high Q (more than 14.6 times higher than a uniform lattice in simulations) and robust BIC. Accompanying with the band folding, certain inaccessible modes in a uniform lattice become accessible at Γ point, and multiple Fano resonances were captured in the hybrid lattice which could enable an alternative approach for broadband molecular fingerprint sensing[12,13].

Materials and Methods

Simulations

Numerical simulations were carried out using commercially available software (COMSOL Multiphysics) with RF module of the finite-element frequency-domain solver. Periodic boundary conditions were employed for the unit cell, and perfectly matching layer (PML) was applied at the input and output ports. A nondispersive refractive index n = 3.45 was set for silicon without loss as substrate. For the calculations of eigenvalues and radiative quality factors, perfect electric conductor (PEC) was used for DSRR. In simulation of transmission spectra, DSRR was set as aluminum with a conductivity of 3.56×10^7 S·m^{-1}.

Fabrications

Prior to fabrication, a 500 μm thick high-resistivity silicon (resistivity > 10000 Ω·cm) wafer was cleaned in an ultrasonic bath with acetone for 10 min and rinsed with isopropanol followed by baking on a hot plate at 120 °C for 180 s. Afterwards, a 2 μm RZJ 304.50 photoresist was spin-coated on the silicon at a speed of 5000 r/s for 30 s. The substrate with photoresist was then baked on a hot plate (100 °C, 180 s). Conventional UV photolithography (SUSS-MA6) was used to transfer DSRR pattern on photoresist, and then the sample was developed with a RZX3038 developer for ~ 30 s. The patterned sample was then baked on a hot plate (120 °C, 90 s). Finally, electron beam evaporation (TF500) was used to deposit 200 nm thick aluminum, and liftoff of the remaining photoresist was done in bath with acetone (60 °C, 30 min).

Measurements

Transmission spectra were measured with a commercially available terahertz time-domain spectroscopic system[29]. After Fourier transform, we obtain transmission spectra of samples (t_s) and references (bare silicon substrate, t_r), and get normalized transmission spectra (t=t_s/t_r). With measured transmission spectra, the total $Q_{\rm tot}$ $\left(\dfrac{1}{Q_{\rm tot}} = \dfrac{1}{Q_{\rm rad}} + \dfrac{1}{Q_{\rm ohm}}\right)$ can be extracted by using Fano line-shape equation[30,31]:

$$T_{\rm Fano} = \left| a_1 + ja_2 + \frac{b}{\omega - \omega_0 + j\gamma_{\rm tot}} \right|^2, \qquad (1)$$

where a_1,a_2 and b are real; $\gamma_{\rm tot}$ is the total radiation rate; ω_0 is the central frequency of resonance. $Q_{\rm tot}$ was

determined by $Q_{tot} = \omega_0/2\gamma_{tot}$. We could retrieve Q_{rad} by estimating Q_{ohm} based on simulations.

Results and discussion

We demonstrate the idea with array of classical DSRRs which could be generalized to other symmetry-protected BIC scenarios without prerequisite of multiple BICs in the band. In the symmetric scenario of DSRR, symmetry-protected BIC is uncoupled to free space exhibiting an infinite radiative Q as illustrated in Fig. 1(a). A common strategy to observe the mode in the far field is to break the symmetry of DSRRs by displacing one gap from the center, and radiative channel of the mode is thus open defined as a quasi-BIC (qBIC)[32]. When the gap position of all the resonators in the metasurface is uniformly displaced (Fig. 1(b)), the well-understood type of BIC is defined as a uniform quasi-BIC (U-qBIC) whose radiative Q depends on α following the inverse quadratic law[33,34]

$$Q_{rad} = m\alpha^{-2}, \tag{2}$$

where α is the asymmetric degree (AD) of DSRR and m is a constant determined by geometric parameters. The AD of DSRR is defined as $\alpha = (l_1 - l_2)/(l_1 + l_2) \times 100\%$, where l_1 and l_2 denote the total lengths of left and right metallic branches of the resonator, respectively (see Fig. 1(d)).

In the scenario of U-qBIC, all the symmetry-breaking resonators contribute to the far-field radiation that follows the inverse quadratic law in Eq. (2). In addition to the general strategy of breaking symmetry to induce U-qBIC, we propose a supercell comprising of metamolecules of hybrid BIC (H_x-BIC, Fig. 1(c)). Radiative loss is reduced in the supercell by suppressing the radiative channel of neighboring resonators along x-axis by recovering them back to C_2 symmetric. When we set the sizes of resonators with l = 60 μm, width w = 8 μm, gap g = 3 μm, and period of square lattice a = 73 μm (Fig. 1(d)), the frequency of fundamental BIC will fall in terahertz regime. Simulated and experimental far-field transmission spectra of the three scenarios are shown in Fig. 1(e) and 1(f), respectively (at α = 4.95% for U-qBIC and H_x-BIC). By comparing BIC, U-qBIC and H_x-BIC in the spectra, we observe the evolution of quasi-BIC as revealed by the Fano resonances in the far field where the resonance cannot be captured for symmetric resonators (α = 0, black line), and appears at 0.52 THz in DSRR with α = 4.95% (red and blue lines) for U-qBIC and H_x-BIC lattices. Quality factors of the Fano resonances were extracted by using Fano fitting (see *Materials and Methods*). A significant improvement of Q is observed from U-qBIC (Q = 10.1) to H_x-BIC (Q = 29.6) in the experiments (Fig. 1(f), from 19.6 to 36.1 in simulations as

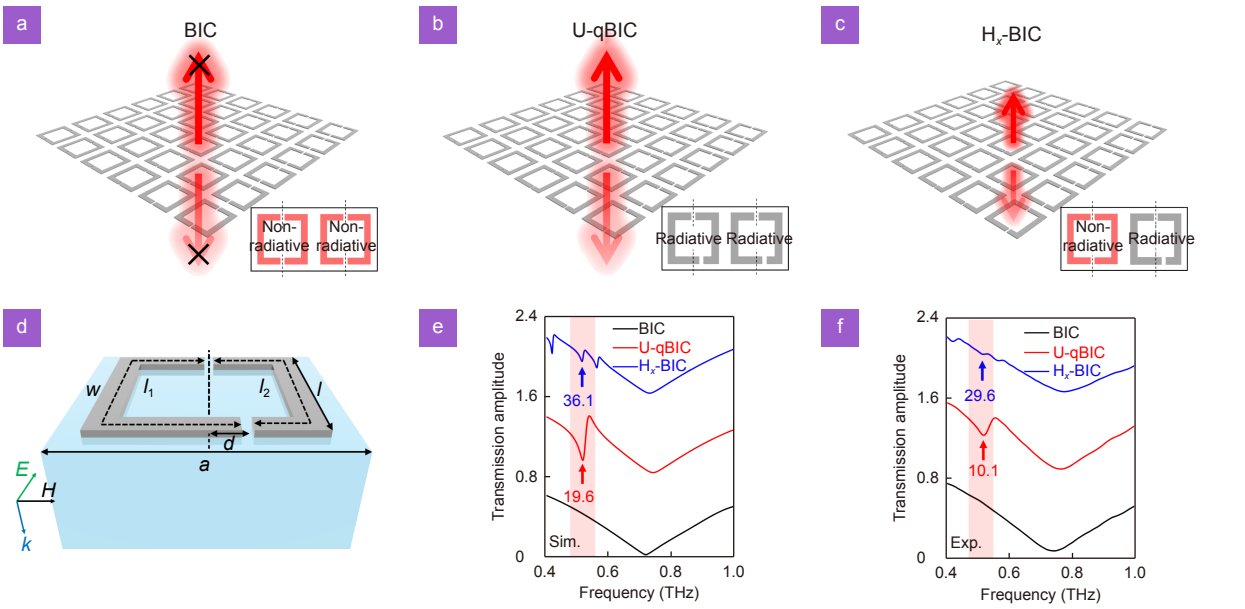

Fig. 1 | Hybrid BIC lattices. (**a**–**c**) Schematic diagram of a symmetry-protected BIC lattice without radiation channel (a), a uniform quasi-BIC lattice with radiation channel open by breaking symmetry of all the resonators (b), and a hybrid quasi-BIC lattice with C_2 symmetry preserved in the neighboring resonators along x-axis in a supercell (c). (**d**) A double gap split ring resonator as the unit cell of the metasurface. (**e**, **f**) Simulated (e) and experimental (f) transmission amplitude spectra for the three-type lattices. The same asymmetry degree (α = 4.95%) was applied for U-qBIC and H_x-BIC metasurfaces.

shown in Fig. 1(e)).

The intuitive evolution of BIC from U-qBIC to H_x-BIC is unambiguously interpreted from the eigenvalue analysis in the reciprocal space. As shown in Fig. 2(a) and 2(b), the period of diatomic supercells is doubled along *x*-axis compared with monoatomic one (with $\alpha = 0$ to obtain the intrinsic properties), and the corresponding BZ is thus folded accordingly in Γ-X direction as indicated in Fig. 2(c). The outer black square and inner orange rectangle describe the BZ of monoatomic and diatomic lattices, respectively. The energy dispersion surfaces have inversion symmetry in BZ, and thus the eigenvalues in blue and white-colored areas are equivalent as determined by the time-reversal symmetry[35]. Such a unique property leads to a folding BZ of diatomic lattice from monoatomic lattice, and modes at the edge of the unfolded BZ (X and M points) in monoatomic lattice are folded to Γ and Y points[34,36,37].

The mode evolution in the band folding process was verified with eigenmode analysis in simulations with DSRRs at $\alpha = 0$ to obtain the eigenfrequencies and intrinsic radiative Q of the interested modes (see *Materials and Methods*). In Fig. 2(d), the half bands (k from X'-X) of a monoatomic supercell appear in the band of diatomic supercell that are reflected with respect to the dotted line. Here, band diagram of diatomic supercell was shrunk (indicated by Γ-X', orange lines) to half of monoatomic supercell (Γ-X, black dots) for comparison, but all the modes are included. A coincidence of the BIC band (highlighted by an arrow) occurs between the two supercells but only half band remains in the diatomic supercell. A direct consequence of the band folding

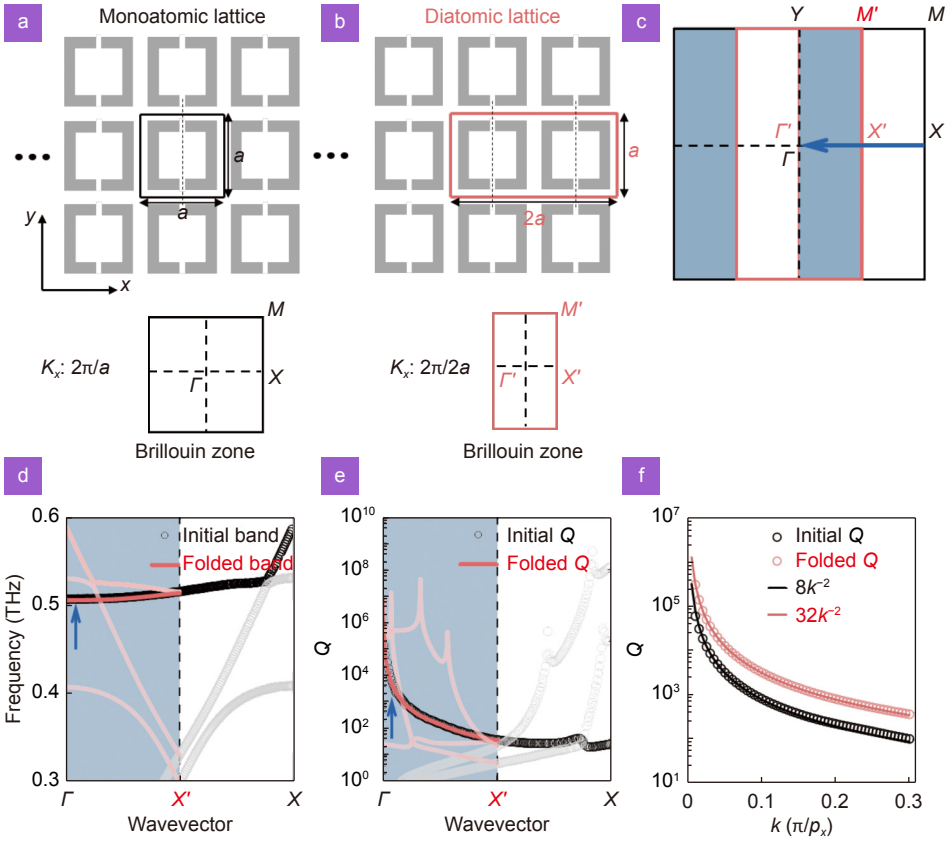

Fig. 2 | Interpretation of hybrid BIC from reciprocal space. (**a**, **b**) Brillouin zones of monoatomic and diatomic supercells at $\alpha = 0$ when the periods were chosen with *a* and 2*a* in the *x* direction. (**c**) Illustration of Brillouin zones for monoatomic and diatomic supercells showing the band folding operation where X and M points in the BZ of a monoatomic supercell are folded to X' and M' points in the BZ of a diatomic supercell, and Γ(Γ') point is fixed. (**d**) Band diagrams of monoatomic (black circles) and diatomic (orange lines) supercells showing the folding behavior where all the modes of a monoatomic supercell in unshaded region are reflected into the shaded region representing modes of a diatomic supercell. (**e**) Radiative quality factors of monoatomic and diatomic supercells. The same folding behavior of Q is inherited from the eigenmodes. (**f**) Comparison of radiative Q versus k between monoatomic and diatomic supercells. Circles are simulated values and solid lines are fitting curves with Eq. (2) whose coefficient is 4-times larger in a diatomic supercell than that of a monoatomic supercell. Here, p_x is period of supercell along *x* direction. Perfect electric conductor (PEC) was used for DSRRs in simulations to calculate eigenvalues and quality factors.

process is that the otherwise inaccessible modes at X point in a monoatomic supercell become leaky at Γ point of diatomic supercell which could thus be observed as multiple Fano resonances in the far field (as revealed by the Fano resonances in blue lines of Fig. 1(e) and 1(f)). The accompanying radiative Q of the modes inherit the same folding properties in BZ (Fig. 2(e)), and discards the half band with lower Q at larger wavevectors in a monoatomic supercell (folded as a new band in the BZ of diatomic supercell) whose radiative Q and k relationship still follows Eq. (2). The half band with higher Q is expanded to fill the full BZ of diatomic supercell (Fig. 2(f)). A direct comparison reveals a 4-time increase of quality factors in a diatomic supercell than that in a monoatomic supercell as verified by the numerical fitting via Eq. (2) as a consequence of the folding and expanding process.

The above discussions could be numerically and experimentally demonstrated via far-field measurements by breaking the symmetry of the resonators (i.e., $\alpha \neq 0$) which shifts BIC to quasi-BIC at Γ point (Fig. 3(a) and 3(b)). All the resonators are asymmetric in U-qBIC lattice (monoatomic supercell) with a period of a, while H_x-BIC lattice (diatomic supercell) is constructed by restoring C_2 symmetry of the neighboring resonators in the diatomic supercell so that the period along x direction is $2a$ (Fig. 3(b)). Far-field transmission spectra were calculated at normal incidence (along z direction) using COMSOL Multiphysics (see *Materials and Methods*), and quasi-BIC was captured as a classical Fano lineshape in Fig. 3(c) (at α= 2.97%). For H_x-BIC lattice, additional Fano resonances appear in addition to the original one as a consequence of band folding originating from X point of U-qBIC supercell (right panel of Fig. 3(c), also refer to Supplementary materials for the features of these resonances). Although the band dispersion coincides between U-qBIC and H_x-BIC supercells for the quasi-BIC mode, their radiative Q versus k relationship reveals a divergence (Supplementary Fig. S1), and the fitting curves still follow the inverse quadratic law but with different coefficients due to the involvement of geometrical asymmetry. The band folding and expansion processes lead to a significant improvement of Q of Fano resonances at 0.504 THz from (U-qBIC) to (H_x-BIC). For asymmetric resonators, radiative Q versus α relationship reveals similar inverse quadratic dependence as that of radiative Q versus k, and significant improvement of Q values and larger robustness against variation of α are obtained in a H_x-BIC supercell (Fig. 3(d)).

We fabricated the samples with conventional photolithography, and the microscopic images of samples are shown in Fig. 3(a) and 3(b). The transmission spectra were measured with terahertz time-domain spectroscopy (THz-TDs) system. Typical spectral features of Fano resonances were captured in experiments except the overall lower quality factors and weaker resonant features (Fig. 3(e)) that are attributed to the intrinsic losses of metallic resonators, finite number of excited resonators, limited scan length (40 ps) and signal to noise ratio of the experimental setup. We designed the samples at a larger asymmetry degree of 7.42% so that the quality factor falls within the instrumental resolution. The same interpretation could be simply generalized to H_y-BIC lattice which folds the band of Γ-Y (see Supplementary Fig. S2 with detailed band analysis, simulations, and experiments) and H_d-BIC lattice which folds the band of Γ-M (see Supplementary Fig. S3).

With the interpretation of band folding in the hybrid lattice, we could further expand the scheme to high order in the BZ by introducing a diagonal nonradiative resonators in the 2×2 supercells. In this scenario, two configurations, where one (Fig. 4(a), H_q-BIC) and three (Fig. 4(b), H_t-BIC) out of the four resonators in a supercell preserve C_2 symmetry, will share exactly the same band diagram (middle panel of Fig. 4(d)) folded from that of U-qBIC supercell. However, their Q will exhibit a striking divergence as a result of different radiation densities (see Supplementary Fig. S4). The calculated band diagram and transmission spectra are shown in Fig. 4(d) where seven Fano resonances are observed for both H_q-BIC and H_t-BIC lattices at $\alpha = 2.97\%$. Fano frequencies match with mode frequencies at Γ point in the reciprocal space where all the modes are folded from X (red circles), Y (orange circles), and M (blue circles) points except the original black line. Despite the same band diagram, a significantly narrower linewidth is observed at 0.504 THz for H_q-BIC supercell due to the lower radiative density than that of H_t-BIC (highlighted resonances in Fig. 4(d)). It is noted that the significant improvement of radiative Q in H_q-BIC supercell occurs only in the vicinity of Γ, and gradually converges to overlap with H_t-BIC supercell at off-Γ points in reciprocal space since all the resonators gradually increase radiation at large wavevectors (see supplementary Fig. S4(c) for a detailed analysis). Samples with H_q-BIC and H_t-BIC lattices at $\alpha = 7.42\%$ (Fig. 4(a) and 4(b)) were fabricated and measured with far-field transmission spectra as shown in Fig. 4(e). A

larger asymmetry degree was applied in the samples for measurements since the limited resolution and signal to noise ratio of THz-TDs led to the difficulty in capturing the very high-*Q* resonances. All the seven Fano resonances can be captured but reveal weak spectral signatures as a result of finite number of supercells with inevitable Ohmic losses as compared to the infinite array in simulations.

Symmetry-protected BICs have found a plethora of important applications in lasing, nonlinear optics, terahertz generation, and biosensors. Significant improvement of light-matter interactions could be obtained with these BICs that have enabled lower lasing threshold, higher-efficiency generation of harmonics and terahertz

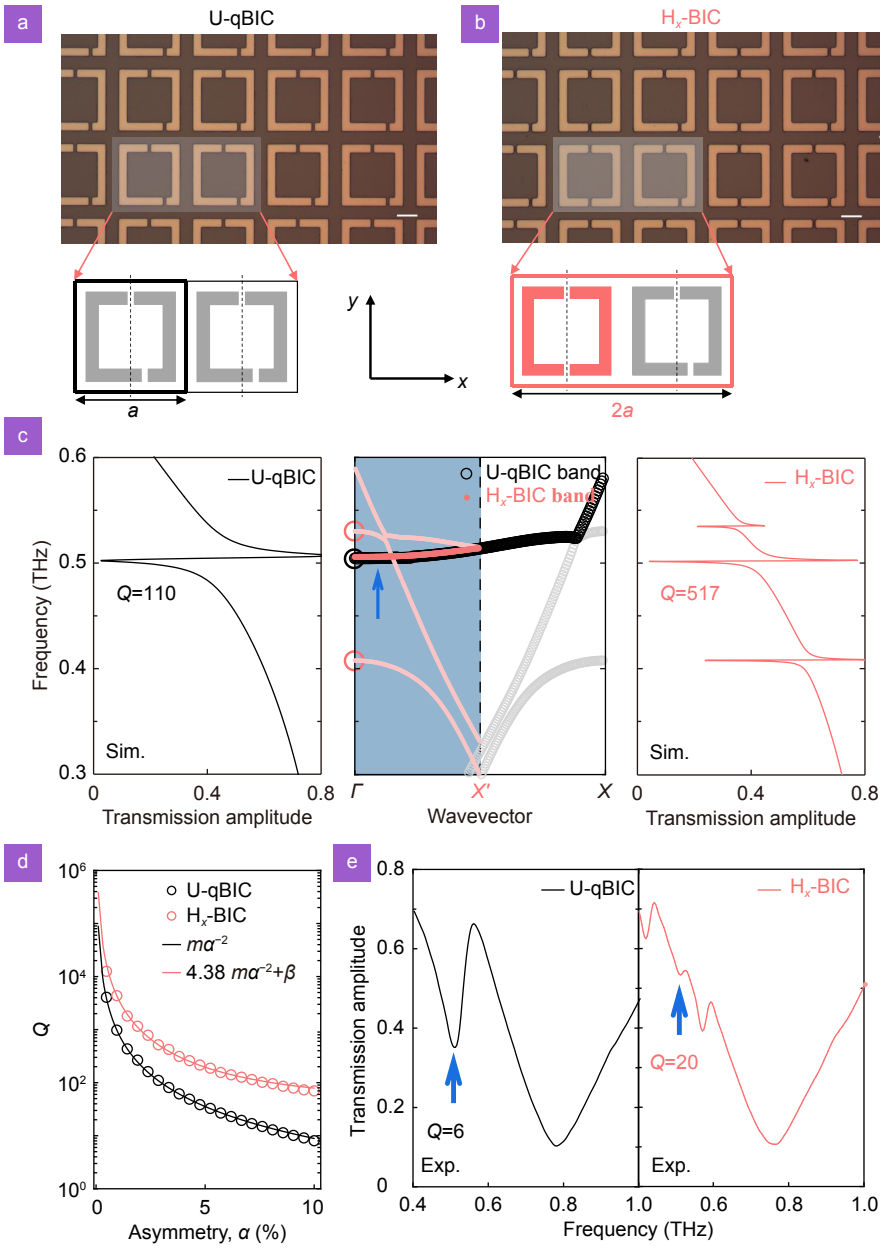

Fig. 3 | Experimental demonstration of the high-*Q* hybrid BIC. (**a**, **b**) Microscopic images of U-qBIC and H_x-BIC metasurfaces. Supercells of U-qBIC and H_x-BIC metasurfaces are shown in the inset. Scale bar, 20 μm. (**c**) Simulated transmission amplitude spectra of U-qBIC (left) and H_x-BIC (right) metasurfaces at an asymmetry degree of 2.97% with excitation electric field polarized along *y*-axis. Band diagrams of U-qBIC and H_x-BIC supercells are shown in the middle. (**d**) Simulated radiative *Q* (circles) versus asymmetry degree (α) with inverse quadratic fitting curves (solid lines) of U-qBIC (black) and H_x-BIC (orange) supercells. Here, an additional constant of β is necessary to account for the nonuniform asymmetry in the hybrid lattice. (**e**) Experimental transmission amplitude spectra of U-qBIC and H_x-BIC metasurfaces at an asymmetry degree of 7.42% with excitation electric field polarized along *y*-axis. The linewidth of Fano resonances is larger than that of simulations due to Ohmic loss in metallic resonators (aluminum) and finite number of supercells.

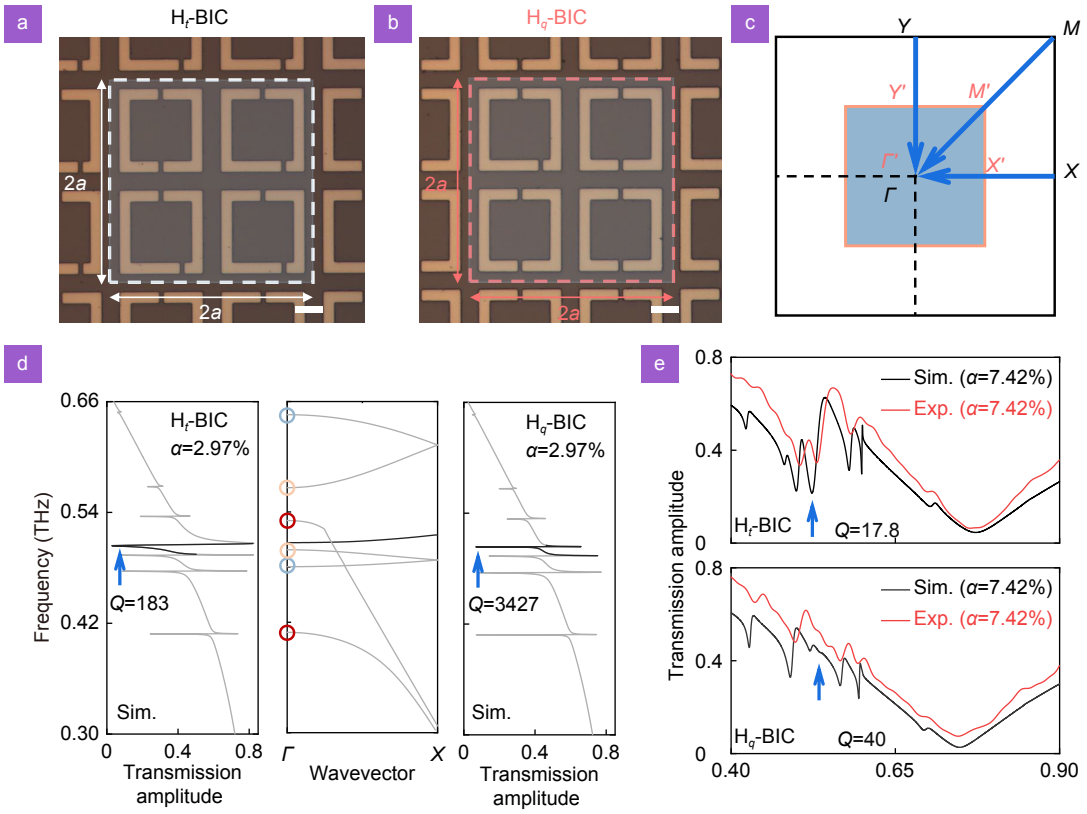

Fig. 4 | Generalized high-order hybrid BICs. (**a**, **b**) Microscopic images of H_t-BIC and H_q-BIC metasurfaces with three and one asymmetric resonators out of four in a 2×2 supercell, respectively, and the period is 2*a* along both *x* and *y* axes. Scale bar, 20 μm. (**c**) Schematic diagram of band folding from U-qBIC lattice (black) to H_t-BIC/H_q-BIC (red) in the Brillouin zone. (**d**) Simulated transmission amplitude spectra of the H_t-BIC (left) and H_q-BIC (right) metasurfaces at an asymmetry degree of 2.97%. The band structure of H_t-BIC/H_q-BIC is shown in the middle, and the modes at the *Γ* point marked with different colored circles are folded from *X* (red), *Y* (orange), and *M* (blue) points in the Brillouin zone of U-qBIC lattice, respectively. The highlighted resonances show the original modes inherited from U-qBIC lattice. (**e**) Experimental (orange) and simulated (black) transmission amplitude spectra of H_t-BIC and H_q-BIC metasurfaces at an asymmetry degree of 7.42%. The overall linewidth of Fano resonances is larger than that of simulations due to Ohmic loss in metallic resonators (aluminum) and finite number of supercells.

radiations, and hyperspectral sensing. Traditionally, most common logic to access a quasi-BIC is to break the symmetry in the level of resonator itself. In this work, we have introduced a different approach to tailor the radiative losses from the level of the entire lattice. Via selectively preserving the C_2 symmetry of resonators in the supercell in a hybrid BIC lattice, we can reduce the radiation density and thus effectively improve the overall quality factors. We numerically and experimentally investigated four-type typical hybrid lattices via investigating 0/4 (U-qBIC), 1/4 (H_t-BIC), 2/4 ($H_{x/y/d}$-BIC), and 3/4 (H_q-BIC) supercells, and found a progressive increase of the overall quality factors (Fig. 5(a)). The retrieved Q_{rad} from experiments reveals a good agreement with simulations and theory. An amplification coefficient of 14.6 of Q_{rad} in H_q-BIC supercell (Q = 59363) is observed compared with that in U-qBIC lattice (Q = 4062) at a fixed asymmetry degree of α = 0.495% (theoretically 16 times from band folding analysis), and a larger contrast is observed at larger asymmetry degrees. Meanwhile, the H_q-BIC lattice exhibits strong immunity to symmetry breaking (see Fig. 5(a)), with the Q changing very slowly as the degree of symmetry breaking increases. In particular, the quality factors are stable at a large value when AD exceeds 3%. This reveals a clue of saturation of radiative Q at larger asymmetries which guarantees that it will not deteriorate due to the fabrication imperfection or disorders.

A common fabrication imperfection in photolithography and E-beam lithography is the rounded angles in the square or rectangular resonators instead of the designed right angles. The radius (r) of rounded angles is usually impossible to be accurately predicted which will thus deteriorate the very sensitive high-Q resonances as shown in Fig. 5(b) for U-qBIC and H_t-BIC supercells. However, the robustness of quality factors is better in

H_x-BIC and H_q-BIC lattices that will guarantee high-quality factors to a large extent. It is noted that the saturation of radiative Q in H_q-BIC lattice enables an obvious increase of quality factors at a larger defect radius. Simulated transmission spectra of samples with different rounded angles are shown in Supplementary Fig. S5.

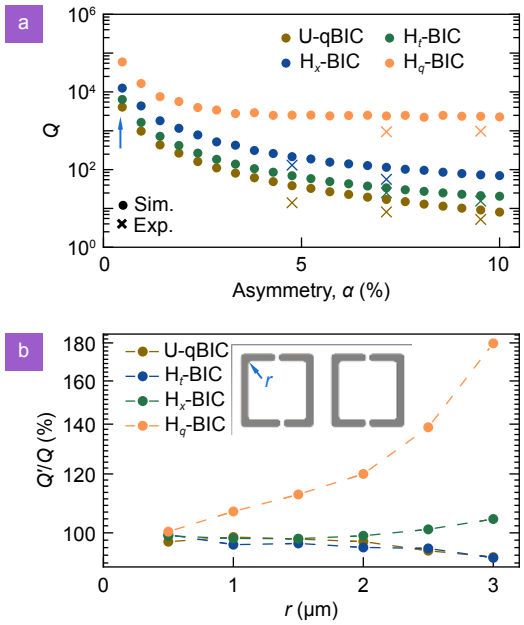

Fig. 5 | Significant *Q* improvement in hybrid BIC supercells and robustness against fabrication imperfections. (**a**) Evolution of radiative Q versus AD for U-qBIC, H_t-BIC, H_x-BIC, and H_q-BIC supercells. The overall quality factors are improved in hybrid supercells with a lower radiation density. (**b**) Influences of fabrication imperfection on quality factors in the four scenarios. Imperfection is introduced by adjusting the sharp right-angle of square in the resonators to rounded angles indicated by radius *r*. *Q* and *Q*′ indicate radiative quality factors for lattices with right-angle and rounded-angle resonators, respectively.

Conclusion

In summary, we report a generalized approach to improve quality factors of symmetry-protected BICs with hybrid BIC supercells. A progressive improvement of overall quality factors is observed in the four-type hybrid supercells, and high-quality factors insensitive to asymmetry degree were realized in the H_q-BIC supercell which guarantees robust resonances with high-quality factors to fabrication defects and disorders. The underlying physics is interpreted from reciprocal space, which uncovers the origin of the stable and improved quality factors of hybrid BIC supercells from band folding process in the Brillouin zone. The consequent multiple Fano resonances at Γ point accompanied with band folding provide an excellent solution for hyperspectral sensing and would be useful for high quality applications in optoelectronic devices. The hybrid BIC supercells exhibit great robustness to fabrication imperfections and disorders and would release the rigid requirements of fabrication accuracy, especially for applications requiring extremely precise quality factors.

References

1. Zhang XD, Liu YL, Han JC, Kivshar Y, Song QH. Chiral emission from resonant metasurfaces. *Science* **377**, 1215–1218 (2022).
2. Kodigala A, Lepetit T, Gu Q, Bahari B, Fainman Y et al. Lasing action from photonic bound states in continuum. *Nature* **541**, 196–199 (2017).
3. Huang C, Zhang C, Xiao SM, Wang YH, Fan YB et al. Ultrafast control of vortex microlasers. *Science* **367**, 1018–1021 (2020).
4. Zhao AK, Jiang N, Peng JF, Liu SQ, Zhang YQ et al. Parallel generation of low-correlation wideband complex chaotic signals using CW laser and external-cavity laser with self-phase-modulated injection. *Opto-Electron Adv* **5**, 200026 (2022).
5. Song JH, Van De Groep J, Kim SJ, Brongersma ML. Non-local metasurfaces for spectrally decoupled wavefront manipulation and eye tracking. *Nat Nanotechnol* **16**, 1224–1230 (2021).
6. Overvig AC, Malek SC, Yu NF. Multifunctional nonlocal metasurfaces. *Phys Rev Lett* **125**, 017402 (2020).
7. Koshelev K, Bogdanov A, Kivshar Y. Meta-optics and bound states in the continuum. *Sci Bull* **64**, 836–842 (2019).
8. Koshelev K, Kruk S, Melik-Gaykazyan E, Choi JH, Bogdanov A et al. Subwavelength dielectric resonators for nonlinear nanophotonics. *Science* **367**, 288–292 (2020).
9. Liu ZJ, Wang JY, Chen B, Wei YM, Liu WJ et al. Giant enhancement of continuous wave second harmonic generation from few-layer GaSe coupled to high-*Q* quasi bound states in the continuum. *Nano Lett* **21**, 7405–7410 (2021).
10. Shi T, Deng ZL, Geng GZ, Zeng XZ, Zeng YX et al. Planar chiral metasurfaces with maximal and tunable chiroptical response driven by bound states in the continuum. *Nat Commun* **13**, 4111 (2022).
11. Liu ZJ, Xu Y, Lin Y, Xiang J, Feng TH et al. High-*Q* quasibound states in the continuum for nonlinear metasurfaces. *Phys Rev Lett* **123**, 253901 (2019).
12. Yesilkoy F, Arvelo ER, Jahani Y, Liu MK, Tittl A et al. Ultrasensitive hyperspectral imaging and biodetection enabled by dielectric metasurfaces. *Nat Photonics* **13**, 390–396 (2019).
13. Tittl A, Leitis A, Liu MK, Yesilkoy F, Choi DY et al. Imaging-based molecular barcoding with pixelated dielectric metasurfaces. *Science* **360**, 1105–1109 (2018).
14. Ra'di Y, Krasnok A, Alù A. Virtual critical coupling. *ACS Photonics* **7**, 1468–1475 (2020).
15. Zhang N, Wang YJ, Sun WZ, Liu S, Huang C et al. High-*Q* and highly reproducible microdisks and microlasers. *Nanoscale* **10**, 2045–2051 (2018).
16. Moiseev EI, Kryzhanovskaya N, Polubavkina YS, Maximov MV, Kulagina MM et al. Light outcoupling from quantum dot-based microdisk laser via plasmonic nanoantenna. *ACS Photonics* **4**, 275–281 (2017).

17. Koschorreck M, Gehlhaar R, Lyssenko VG, Swoboda M, Hoffmann M et al. Dynamics of a high-Q vertical-cavity organic laser. *Appl Phys Lett* **87**, 181108 (2005).
18. Suh W, Wang Z, Fan SH. Temporal coupled-mode theory and the presence of non-orthogonal modes in lossless multimode cavities. *IEEE J Quantum Electron* **40**, 1511–1518 (2004).
19. Hsu CW, Zhen B, Lee J, Chua SL, Johnson SG et al. Observation of trapped light within the radiation continuum. *Nature* **499**, 188–191 (2013).
20. Zhen B, Hsu CW, Lu L, Stone AD, Soljačić M. Topological nature of optical bound states in the continuum. *Phys Rev Lett* **113**, 257401 (2014).
21. Fang CZ, Yang QY, Yuan QC, Gan XT, Zhao JL et al. High-Q resonances governed by the quasi-bound states in the continuum in all-dielectric metasurfaces. *Opto-Electron Adv* **4**, 200030 (2021).
22. Yuan LJ, Lu YY. Bound states in the continuum on periodic structures: perturbation theory and robustness. *Opt Lett* **42**, 4490–4493 (2017).
23. Minkov M, Dharanipathy UP, Houdré R, Savona V. Statistics of the disorder-induced losses of high-Q photonic crystal cavities. *Opt Express* **21**, 28233–28245 (2013).
24. Taghizadeh A, Chung IS. Quasi bound states in the continuum with few unit cells of photonic crystal slab. *Appl Phys Lett* **111**, 031114 (2017).
25. Jin JC, Yin XF, Ni LF, Soljačić M, Zhen B et al. Topologically enabled ultrahigh-Q guided resonances robust to out-of-plane scattering. *Nature* **574**, 501–504 (2019).
26. Kang M, Mao L, Zhang SP, Xiao M, Xu HX et al. Merging bound states in the continuum by harnessing higher-order topological charges. *Light:Sci Appl* **11**, 228 (2022).
27. Hwang MS, Lee HC, Kim KH, Jeong KY, Kwon SH et al. Ultralow-threshold laser using super-bound states in the continuum. *Nat Commun* **12**, 4135 (2021).
28. Liu DJ, Yu X, Wu F, Xiao SY, Itoigawa F et al. Terahertz high-Q quasi-bound states in the continuum in laser-fabricated metallic double-slit arrays. *Opt Express* **29**, 24779–24791 (2021).
29. Cong LQ, Singh R. Spatiotemporal dielectric metasurfaces for unidirectional propagation and reconfigurable steering of terahertz beams. *Adv Mater* **32**, 2001418 (2020).
30. Yang YM, Kravchenko II, Briggs DP, Valentine J. All-dielectric metasurface analogue of electromagnetically induced transparency. *Nat Commun* **5**, 5753 (2014).
31. Kang M, Zhang ZY, Wu T, Zhang XQ, Xu Q et al. Coherent full polarization control based on bound states in the continuum. *Nat Commun* **13**, 4536 (2022).
32. Cong LQ, Singh R. Symmetry-protected dual bound states in the continuum in metamaterials. *Adv Opt Mater* **7**, 1900383 (2019).
33. Koshelev K, Lepeshov S, Liu MK, Bogdanov A, Kivshar Y. Asymmetric metasurfaces with high-Q resonances governed by bound states in the continuum. *Phys Rev Lett* **121**, 193903 (2018).
34. Overvig AC, Shrestha S, Yu NF. Dimerized high contrast gratings. *Nanophotonics* **7**, 1157–1168 (2018).
35. Vaity P, Gupta H, Kala A, Dutta Gupta S, Kivshar YS et al. Polarization-independent quasibound states in the continuum. *Adv Photonics Res* **3**, 2100144 (2022).
36. Overvig AC, Malek SC, Carter MJ, Shrestha S, Yu NF. Selection rules for quasibound states in the continuum. *Phys Rev B* **102**, 035434 (2020).
37. Overvig A, Yu NF, Alù A. Chiral quasi-bound states in the continuum. *Phys Rev Lett* **126**, 073001 (2021).

Acknowledgements

This work was supported by the National Natural Science Foundation of China (Award No. 62175099), Guangdong Basic and Applied Basic Research Foundation (Award No. 2023A1515011085), Stable Support Program for Higher Education Institutions from Shenzhen Science, Technology & Innovation Commission (Award No. 20220815151149004), Global recruitment program of young experts of China, and startup funding of Southern University of Science and Technology. The authors acknowledge the assistance of SUSTech Core Research Facilities and thank Yao Wang for helpful discussions on fabrication.

Author contributions

L. Q. Cong initiated the idea and supervised the project. J. X. Fan fabricated samples, performed experiments and simulations, analyzed data, and initiated the manuscript. Z. L. Li performed partial experiments. All authors read and commented on the manuscript. L. Q. Cong, J. Q. Gu, and J. G. Han supervise the project.

Competing interests

The authors declare no competing financial interests.